

A NEW OBSERVATION-BASED CLUMPY TORUS MODEL FOR ACTIVE GALACTIC NUCLEI

X. ZHAO^{1,2}, S. MARCHESI^{1,3}, M. AJELLO¹, D. COLE¹, Z. HU¹
Draft version October 10, 2021

ABSTRACT

The obscuration observed in active galactic nuclei (AGN) is mainly caused by dust and gas distributed in a torus-like structure surrounding the supermassive black hole (SMBH). Recent observations suggest that the obscuring material in the dusty torus is clumpy rather than uniformly distributed. However, most of the AGN models still adopt a smooth torus when characterizing obscuring material surrounding the SMBH. In this work, we perform a broadband X-ray spectral analysis of a large unbiased sample of obscured AGN in the nearby universe which have high-quality archival *NuSTAR* data, enabling us to accurately characterize the physical and geometrical properties of their obscuring tori. We find that different types of AGN may possess similar tori, which are on average Compton thick ($N_{\text{H,tor,ave}} \approx 1.4 \times 10^{24} \text{ cm}^{-2}$) and are significantly clumpy (e.g., for >80% of sources in our sample, their torus average column densities are more than three times different from their line-of-sight column densities). Utilizing the obtained information about the torus column density, torus covering factor, and torus clumpiness for all sources in our sample, we develop a new clumpy torus model of AGN. Using our new model, we predict the observed column density distribution of AGN in the nearby universe, which we find in good agreement with the constraints from recent population synthesis models.

Keywords: galaxies: active – galaxies: nuclei – X-rays: galaxies

1. INTRODUCTION

Active galactic nuclei (AGN) are one of the most powerful objects in the sky due to the extreme accretion process of the super-massive black hole (SMBH) in the center of galaxies (Soltan 1982; Richstone et al. 1998). The material (gas and dust) surrounding the SMBH not only feeds the central monster but is the origin of the obscuration of the AGN (see Hickox & Alexander 2018, for a recent review). Studying the properties of these obscuring material in the AGN is key to understanding the growth of SMBHs. It was suggested by the widely accepted AGN unified model (Antonucci & Miller 1985; Antonucci 1993) that the obscuring material of the AGN is in an optically thick torus-like structure. The obscuring torus was thought to be smooth, however, many recent observations show that the material that makes the torus is clumpy rather than uniformly distributed (see Netzer 2015, for a recent review), e.g., the rapid variabilities and eclipse events found in X-ray observations (e.g., Risaliti et al. 2002; Markowitz et al. 2014) and the observed 10 μm silicate features in the Infrared spectra which cannot be explained by smooth torus (e.g., Nenkova et al. 2002; Mason et al. 2009). Various clumpy torus models were developed in recent years based on Infrared observations (e.g., Hönig et al. 2006; Nenkova et al. 2008; Stalevski et al. 2016) and on X-ray observations (e.g., Matt & Fabian 1994; Liu & Li 2014; Furui et al. 2016; Buchner et al. 2019; Tanimoto et al. 2019). However, notable degeneracy still exist among different models when describing the clumpy torus.

Based on the obscuration of the torus, AGN can be categorized into unobscured when the column density on the line-of-sight is $N_{\text{H,los}} < 10^{22} \text{ cm}^{-2}$, and obscured when $N_{\text{H,los}} > 10^{22} \text{ cm}^{-2}$. The most obscured sources are called Compton thick (CT-) AGN when $N_{\text{H,los}} > 10^{24} \text{ cm}^{-2}$. Moreover, AGN with different levels of obscuration are the main contributors to the cosmic X-ray background (CXB; the diffuse X-ray emission in the universe; e.g., Maccacaro et al. 1991; Madau et al. 1994; Comastri et al. 1995). Several works have studied the column density distribution of AGN using hard X-ray surveys (e.g., Burlon et al. 2011; Ricci et al. 2015), which are more efficient in detecting obscured AGN since high energy photons can more easily penetrate the dense material surrounding the SMBH. However, only a small number of CT-AGN have been discovered so far (e.g., Risaliti et al. 1999), due to their large obscuration, which makes it difficult both to detect them and to properly measure their column density. Consequently, the uncertainties on the measurement of the intrinsic distribution of the column density of AGN are still significant. Significantly, the fraction of CT-AGN predicted by AGN population synthesis models ($\sim 30\text{--}50\%$; Gilli et al. 2007; Ueda et al. 2014; Buchner et al. 2015; Ananna et al. 2019) is much higher than what has been observed so far ($\sim 10\text{--}30\%$; Burlon et al. 2011; Ricci et al. 2015; Lansbury et al. 2017; Zappacosta et al. 2018). Therefore, the intrinsic column density distribution of AGN is still controversial.

In this work, we develop a new AGN torus model, which is based on the broadband X-ray spectral analysis of high-quality data available for a large unbiased sample of obscured AGN in the local universe ($z < 0.15$), and takes into account the clumpy nature of the obscuring torus. In Section 2, we introduce the criteria that are used to select the unbiased AGN sample and describe the X-ray spectral analysis technique. In Sec-

¹ Department of Physics & Astronomy, Clemson University, Clemson, SC 29634, USA

² Harvard-Smithsonian Center for Astrophysics, 60 Garden Street, Cambridge, MA 02138, USA

³ INAF-Osservatorio Astronomico di Bologna, Via Piero Gobetti, 93/3, I-40129, Bologna, Italy

tion 3, we report the spectral analysis results. In Section 4, we build a new AGN clumpy torus model using the obtained tori information. With this model, we derive the line-of-sight column density distribution of the AGN in the nearby universe, which is compared with the results obtained from previous observations and the constraints from different population synthesis models. All reported uncertainties are at 90% confidence level unless otherwise stated. Standard cosmological parameters are adopted as follows: $\langle H_0 \rangle = 70 \text{ km s}^{-1} \text{ Mpc}^{-1}$, $\langle q_0 \rangle = 0.0$ and $\langle \Omega_\Lambda \rangle = 0.73$.

2. SAMPLE SELECTION AND SPECTRAL ANALYSIS

2.1. Selection Criteria

The sources presented in this work are selected from the 100-month Palermo *Swift*/BAT catalog⁴ (Marchesi et al., in preparation), which covers 50% of the sky at the 15–150 keV flux limit of $\sim 5.4 \times 10^{-12} \text{ erg cm}^{-2} \text{ s}^{-1}$. The selection criteria are as follows:

1. Line-of-sight column density between 10^{23} and 10^{24} cm^{-2} . To characterize the physical and geometrical properties of the obscuring material around the SMBH, one needs a clear signature of the reprocessed component of the obscuring torus rather than the line-of-sight component. CT-AGN, which are on average more complex to model, are studied in a separate set of papers (Marchesi et al. 2018, 2019; Zhao et al. 2019a,b, Marchesi et al. in prep.).
2. Available *NuSTAR* data. *NuSTAR* spectra are instrumental to properly characterize the properties of heavily obscured AGN in the local universe due to the significant suppression of their spectra at soft X-rays (see, e.g., Marchesi et al. 2018).

A total of 94 out of ~ 1000 AGN in the BAT catalog have been selected⁵ and analyzed in this work. The median redshift of the sources in our finalized sample is $\langle z \rangle = 0.0273$ (i.e., the median distance is $\langle d \rangle \sim 118 \text{ Mpc}$).

2.2. Spectral Analysis

We perform a broadband (1–78 keV) X-ray spectral analysis of all 92 sources in our sample. *NuSTAR* (3–78 keV) data provide coverage in hard X-ray band. For the soft X-ray band, we utilize archival *XMM-Newton* data when available (1–10 keV; 48 sources), *Chandra* data (1–7 keV; 18 sources) when *XMM-Newton* data are not available, and *Swift-XRT* data (1–10 keV; 27 sources) when neither *XMM-Newton* nor *Chandra* data are available. The details of the data reduction are described in Appendix A. The spectra are fitted using *XSPEC* (Arnaud 1996) version 12.10.0c.

The spectra of heavily obscured AGN is complicated by the emergence of the reprocessed component including the Compton scattering and fluorescent emission lines, which are buried by the line-of-sight component in the unobscured AGN spectra. However, in spite of adding

the difficulty of characterizing the spectra, this reprocessed component becomes a perfect tool to estimate the physical and geometrical properties of the obscuring material around the central SMBH. In this work, following Zhao et al. (2020), we analyze the spectra of the sources in our sample using the self-consistent *borus02* model (Baloković et al. 2018), which optimizes the exploration of the parameter space and has been intensively used to characterize the heavily obscured AGN.

The complete model used in the spectral analysis consists of three components. A line-of-sight component or the absorbed intrinsic continuum, described by a cut-off power law, denoted by *cutoffpl* in *XSPEC*, multiplied by an obscuring component, including both the photoelectric absorption (*zphabs*) and the Compton scattering (*cabs*) effects. A reprocessed component, produced by the obscuring material near the SMBH, including the Compton scattered continuum and fluorescent lines, characterized by *borus02*. A detailed description of the utilization of the *borus02* model is reported in Appendix B. A scattered component, an unabsorbed cut-off power law multiplied by a constant, modeling the fractional AGN emission which is scattered, rather than absorbed by the obscuring material.

The *borus02* model is used in the following *XSPEC* configuration:

$$\begin{aligned} \text{Model} = & \text{constant}_1 * \text{phabs} * (\text{zphabs} * \text{cabs} * \text{cutoffpl} \\ & + \text{borus02} + \text{constant}_2 * \text{cutoffpl}) \end{aligned} \quad (1)$$

where *constant*₁ is the cross-calibration between *NuSTAR* and the soft X-ray observatories, i.e., *XMM-Newton*, *Chandra* and *Swift-XRT*; *phabs* models the Galactic absorption from our Galaxy.

3. RESULTS

The spectra of 94 sources and their best-fit models can be found online⁶. The best-fit results of the spectral analysis, e.g., line-of-sight column density, $N_{\text{H},\text{l.o.s.}}$, torus average column density, $N_{\text{H},\text{tor}}$, cosine of the inclination angle, $\cos(\theta_{\text{inc}})$, torus covering factors, c_f , 2–10 keV flux, Flux_{2-10} , and 2–10 keV intrinsic (absorption-corrected) luminosity, $L_{\text{int},2-10}$ are reported in Appendix B when *XMM-Newton*, *Chandra*, and *Swift-XRT* data are used, respectively. For 15 sources in our sample, the contributions of their reprocessed emission to the overall spectra are marginal, such that the parameters of the reprocessed component, e.g., the torus average column density, inclination angle, and torus covering factor, cannot be constrained at all. Therefore, for those sources, we analyze their spectra using only the line-of-sight component and the scattered component. Besides, we observe line-of-sight column density variabilities in 43 sources, thus we distinguish the line-of-sight column densities measured in different epochs when fitting the spectra of those sources. We use the line-of-sight column density measured in *NuSTAR* epoch in the following discussion. Eight sources in our sample are found to have line-of-sight column density $N_{\text{H},\text{l.o.s.}} < 10^{23} \text{ cm}^{-2}$ or $N_{\text{H},\text{l.o.s.}} > 10^{24} \text{ cm}^{-2}$, thus these sources are excluded in our sample.

Marchesi et al. (2019, hereafter M19) reported the CT-AGN in the nearby universe which are also selected in the

⁴ http://bat.ifc.inaf.it/100m_bat_catalog/100m_bat_catalog_v0.0.htm

⁵ The line-of-sight column densities provided in the BAT catalog are measured using *Swift*-BAT data and soft X-ray data.

⁶ <https://science.clemson.edu/ctagn/project/>

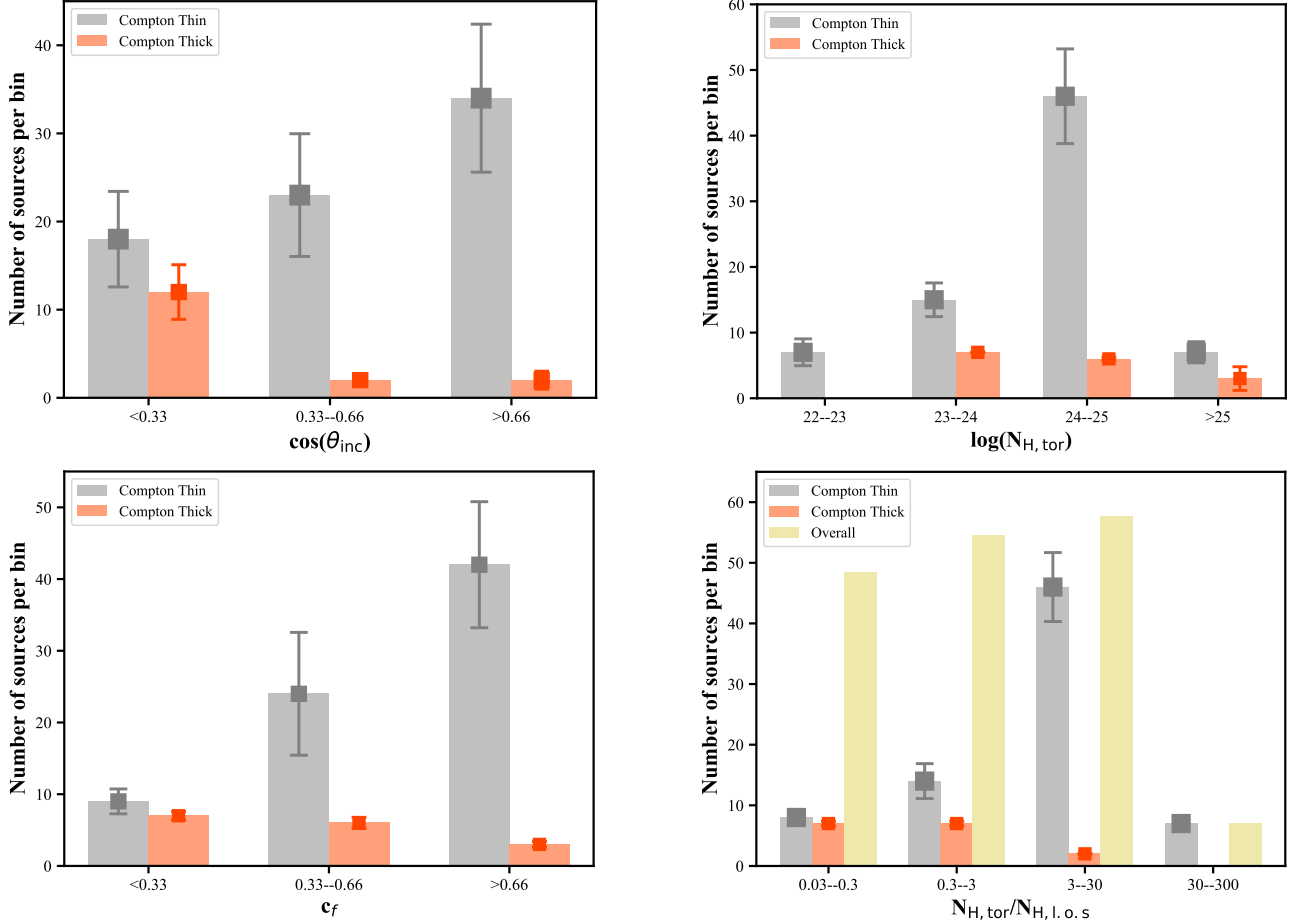


Figure 1. The figures from left to right in the first row and second row are the number of sources with a specific range of the inclination angles, $\cos(\theta_{\text{inc}})$, torus column densities, $\log(N_{\text{H,tor}})$, torus covering factors, c_f , and the torus column density contrast ratio, $N_{\text{H,tor}}/N_{\text{H,l.o.s.}}$, of Compton thin sources in our sample (grey histogram) and CT sources from M19 (orange histogram), respectively. $\cos(\theta_{\text{inc}}) \sim 0.05$ is when the AGN is observed in ‘edge-on’ direction and $\cos(\theta_{\text{inc}}) \sim 0.95$ is when the AGN is observed ‘face-on’. The error bar is at 90% confidence level. The overall torus column density contrast ratio distribution after rescaling is plotted in yellow.

BAT 100-month catalog and have *NuSTAR* data. The sources are analyzed using *borus02* model as well but the inclination angle are fixed at ‘edge-on’ direction when fitting the spectra. We re-analyze these CT sources using the same model presented in Section 2.2 and let the inclination angle free to vary when fitting the spectra, thus we could compare the properties of the obscuring torus of CT sources with those of the Compton thin sources in our sample. The re-analysis results of the CT sources in the M19 sample are reported in the Appendix. Four CT sources in the M19 sample are found to be Compton thin in our re-analysis, therefore, we add those four sources into our Compton thin sample, which in the end includes 92 sources in total⁷. It is worth mentioning that although CT-AGN are ideal sample to study the obscuring torus due to their significantly suppressed line-of-sight emission thus clear signal of the reprocessed emission from the torus, we only use our Compton thin sample to build the new AGN torus model since the CT sample is strongly biased against or incomplete (see, e.g., Fig. 12 in Buron et al. 2011, which shows that the intrinsic number of

CT-AGN is much larger than their observed one). The main results of the spectral analysis are:

- The Compton thin sources in our sample are evenly observed in every direction considering the uncertainties as shown in Fig. 1 (upper left), suggesting that our BAT selected Compton thin AGN sample is an *unbiased* sample. While, most of the CT sources in the M19 sample are observed ‘edge-on’.
- The torus column densities of the Compton thin sources in our sample and CT-AGN in M19 sample are in the $>10^{24} \text{ cm}^{-2}$ range as presented in Fig. 1 (upper right), suggesting that the reflection components produced by CT material are commonly found in the spectra of both Compton thin and CT-AGN. A similar result was also reported in e.g., Buchner et al. (2019).
- The average torus column density is *similar* for both Compton thin and CT-AGN independently on the observing angle, i.e., $\log(N_{\text{H,tor,ave}}) \sim 24.15$, as shown in Fig. 2 (left). We notice that the torus average column density of Compton thin sources

⁷ The median photon indices of the 92 sources is $\langle \Gamma \rangle = 1.69$.

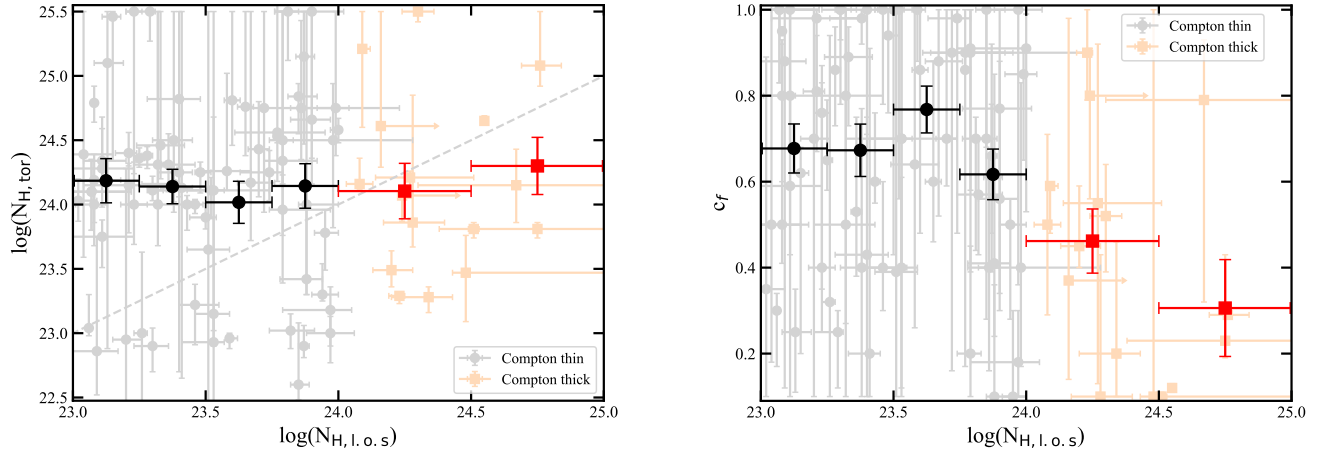


Figure 2. Torus column density $\log(N_{\text{H, tor}})$ (left) and torus covering factor c_f (right) as a function of line-of-sight column density, $\log(N_{\text{H, l.o.s}})$. Compton thin sources are plotted in light grey points while CT sources are plotted in light red squares. The average and 1σ standard error of the torus column densities and torus covering factors in different line-of-sight column density bins are plotted in black points for Compton thin sources and red squares for CT sources, respectively. In the left panel, $\log(N_{\text{H, tor}}) = \log(N_{\text{H, l.o.s}})$ is plotted as a light grey dashed line.

is generally larger than their line-of-sight column density, suggesting that Compton thin AGN are usually observed through an *under-dense* region in their tori; while, the torus average column density of CT-AGN are always smaller than their line-of-sight column density, suggesting that CT-AGN are observed through an *over-dense* region in their tori.

- Compton-thin and CT-AGN have (statistically) different covering factors, with the former having larger ($c_f > 0.5$) covering factors while the latter have smaller ($c_f < 0.5$) covering factors, as shown in Fig. 1 (bottom left). Interestingly, the average torus covering factor of Compton thin AGN is $c_{f,\text{ave}} \sim 0.67$. In contrast, the average torus covering factor decreases significantly when the line-of-sight column density reaches the CT regime, as shown in Fig. 2 (right). Such a trend in CT-AGN has been observed also in e.g., Ricci et al. (2015). It is important to keep in mind, however, that we cannot exclude the possibility that this is a selection bias that the detection of CT-AGN with a large covering factor is more difficult due to their low flux, thus most of the observed CT-AGN have small covering factors.
- The obscuring material in the torus of AGN is *significantly clumpy*. The torus average column densities of the majority of Compton thin and CT-AGN are at least three times different from their line-of-sight column densities as shown in Fig. 1 (bottom right). Moreover, for $\sim 30\%$ of sources in the sample, their torus average column densities are more than ten times different from their line-of-sight column densities.
- The distributions of the torus column density contrast ratio ($\text{CR} = N_{\text{H, tor}}/N_{\text{H, l.o.s}}$) observed in Compton thin and CT-AGN are different (see, Fig. 1 bottom right). We consider that the overall distribution of the torus column density contrast ratio of different types of AGN should be a

combination of the distribution of both the Compton thin AGN and CT-AGN. To combine the two distributions, we rescale the torus column density contrast ratio distribution of CT-AGN before we produce the overall distribution, since we are biased against the detection of CT-AGN, i.e., we need to consider the intrinsic number of Compton thin and CT-AGN. Here, we assume that the number of Compton thin AGN and CT-AGN are similar (see, Fig 1 bottom right), which is in agreement with previous works and what we find in this work, as we will further discuss in Section 4.1. After rescaling, we find that the torus column density contrast ratio is rather flat over the range $\text{CR} = [0.03, 30]$, suggesting that an AGN with a particular torus column density has equal probability to be observed at different line-of-sight column densities.

4. A NEW CLUMPY TORUS MODEL

We find that Compton thin and CT-AGN might possess tori with similar properties, but we observe them through under/over dense regions of the tori. Therefore, the tori properties derived in the previous section allow us to propose a new torus model. The main components of the model are as follows:

1. We assume that the torus column density distribution of AGN has an average of $\log(N_{\text{H, tor,ave}}) \sim 24.15$ with 1σ standard error of $\sim 20\%$ as detailed in Sec. 3 and Fig. 2 (left).
2. We assume that the fraction of unobscured AGN is $\sim 33\%$ due to the fact that the derived torus geometrical covering factor (where the line-of-sight intersects the obscuring material) is ~ 0.67 as shown in Fig. 2 (right).
3. We assume that one's line-of-sight passes through an over-density or under-density region of the obscuring torus with CR in the range of $[0.03-30]$ with equal probability (only a small fraction of sources have even extremely clumpy torus CR outside of this range) as shown in Fig. 1 (bottom right).

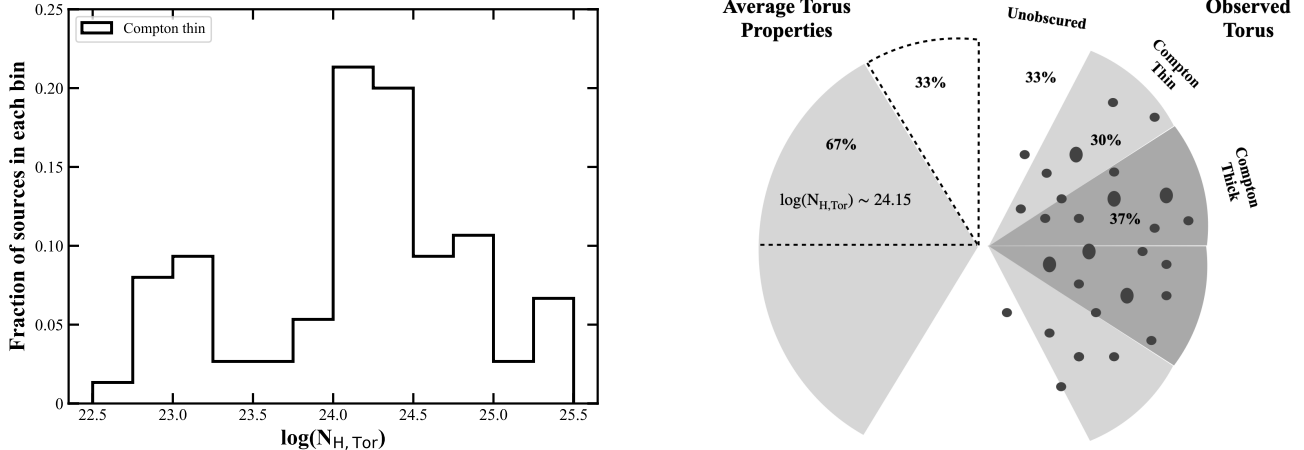


Figure 3. Left: Torus average column density distribution of the sources in our unbiased Compton thin AGN sample. The histogram describes the same sample as in the upper right panel of Fig. 1 but with different grouping bins. Right: The left part of the figure presents that the average torus properties of our unbiased Compton thin sample; The right part of the figure illustrates the AGN line-of-sight column density distribution derived from the torus average column density distribution when the clumpiness of the torus is considered.

4.1. Observed Column Density Distribution of AGN

To derive the observed column density distribution we use the elements of the new clumpy torus model in Sec. 4 and a Monte Carlo method as follows:

1. We draw randomly a torus average column density $N_{\text{H}, \text{tor}}$ from the distribution shown in Fig. 3 (left);
2. We then assign a random CR in the range of [0.03–30] to each $N_{\text{H}, \text{tor}}$, thus the line-of-sight column density of each torus is $N_{\text{H}, \text{l.o.s.}} = N_{\text{H}, \text{tor}}/\text{CR}$;
3. Finally, for 33% of the cases where the line-of-sight does not intersect the torus, we assume that the probability of obtaining a $N_{\text{H}, \text{l.o.s.}}$ between 10^{20} and 10^{22} cm^{-2} is equal.

Fig. 4 and Table 1 compare the obtained line-of-sight column density distribution to previous observations and models.

A discrepancy of the line-of-sight column density distribution between the previous observational results obtained using the *Swift*-BAT (e.g., Burlon et al. 2011; Ricci et al. 2015) and constraints from different population synthesis models (e.g., Gilli et al. 2007; Ueda et al. 2014; Buchner et al. 2015; Ananna et al. 2019) still exists. We compare our derived line-of-sight column density distribution with their results⁸ in Table 1 and in Fig. 4.

When compared to *Swift*-BAT observations, we find that our model predicts a larger number of CT-AGN. This is likely due to the fact that *Swift*-BAT does not detect any AGN at $N_{\text{H}, \text{l.o.s.}} > 10^{25} \text{ cm}^{-2}$. Our predictions are in good agreement with the results of models, particularly those of Ueda et al. (2014). It is worth noting that the column density distribution is luminosity (and possibly redshift dependent, see, e.g., Ananna

⁸ The reported observational column density distributions are those which have been corrected for selection bias and for the bias against detecting extremely absorbed sources. The average redshift of the sources in the samples used in Burlon et al. (2011) and Ricci et al. (2015) are $\langle z \rangle = 0.03$ and 0.055, respectively.

Table 1
Line-of-sight column density distribution from our clumpy torus model. Previous results from observational works, as well as from population synthesis models, are also reported.

	$10^{20}-10^{22}$	$10^{22}-10^{26}$	$10^{22}-10^{24}$	$10^{24}-10^{26}$
Our work	33%	67%	30%	37%
Observations				
Burlon+11	38%	62%	43%	19%
Ricci+15	22%	78%	46%	32%
population synthesis model				
Gilli+07	13%	87%	42%	45%
Ueda+14	33%	67%	34%	33%
Buchner+15	25%	75%	37%	38%
Ananna+19	9%	91%	41%	50%

et al. 2019), and different works adopt different sample of AGN with different luminosity and redshift range to derive the column density distribution. In particular, our work provides a constraint on the line-of-sight column density distribution which is restricted to the AGN with median 2–10 keV intrinsic luminosity of $\langle L_{\text{int}, 2-10} \rangle = 10^{43} \text{ erg s}^{-1}$ in the local Universe ($z < 0.15$).

A schematic of the new observationally-based clumpy torus model itself is illustrated in the right panel of Fig. 3. On the left side of the figure, we present the average torus properties obtained from our unbiased sample, and on the right, we plot the observed torus predicted by our new model when the clumpiness effect is considered.

5. CONCLUSION

We study the obscuring torus of AGN by analyzing the broadband X-ray spectra of a large and unbiased sample of obscured AGN in the nearby universe. We find

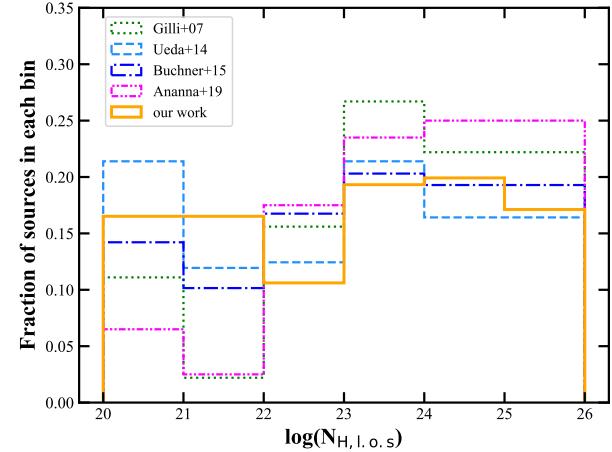
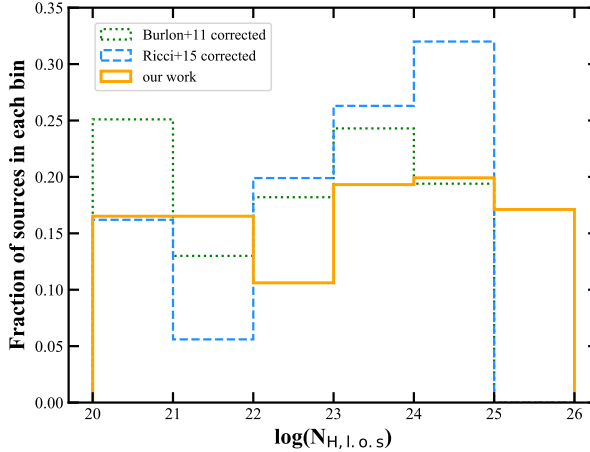


Figure 4. Comparison between the line-of-sight column density distribution derived using our new, observationally-based clumpy torus model with previous observational results (left) and those used in different population synthesis models (right). The extremely obscured sources with $\log(N_{\text{H}, \text{l.o.s.}}) > 26$ are included in the $25 < \log(N_{\text{H}, \text{l.o.s.}}) < 26$ bin.

that Compton thin and CT-AGN may possess similar tori, whose average column density is Compton thick, but they are observed through the different (under-dense or over-dense) regions of the tori. The average torus covering factor of the Compton thin sample is $c_f = 0.67$, suggesting that the fraction unobscured AGN is $\sim 33\%$. In this work, we build a new clumpy torus model of AGN based on the results of our spectral analysis. Using our new model, we derive the line-of-sight column density distribution of AGN in the nearby universe, which is in good agreement with the recent AGN population synthesis models. Our new AGN torus model may help understand the properties of the obscuring materials surrounding the SMBH in the local universe and help constrain the future population synthesis study of CXB. In the future, new X-ray missions such as *Athena* and the proposed *Lynx* and *AXIS* facilities will detect a large sample of obscured AGN at high redshift (see, e.g., Marchesi et al. 2020), which could help us to further study the evolution of the AGN obscuration and the SMBH growth over the cosmic time.

X.Z., M.A. and S.M. acknowledge NASA funding under contract 80NSSC17K0635 and 80NSSC19K0531. X.Z. also acknowledge NASA funding under contract 80NSSC20K0043. This research has made use of the Palermo BAT Catalogue and database operated at INAF-IASF Palermo. We thank the *NuSTAR* Operations, Software and Calibrations teams for support with these observations. This research has made use of data and/or software provided by the High Energy Astrophysics Science Archive Research Center (HEASARC), which is a service of the Astrophysics Science Division at NASA/GSFC and the High Energy Astrophysics Division of the Smithsonian Astrophysical Observatory. This work is based on observations obtained with *XMM-Newton*, an ESA science mission with instruments and contributions directly funded by ESA Member States and NASA. The scientific results reported in this article are based in part on observations made by data obtained from the *Chandra* Data Archive. This work made use of data supplied by the UK *Swift* Science Data Centre at

the University of Leicester.

REFERENCES

Ananna, T. T., Treister, E., Urry, C. M., et al. 2019, *The Astrophysical Journal*, 871, 240
 Anders, E. & Grevesse, N. 1989, *Geochimica et Cosmochimica Acta*, 53, 197
 Antonucci, R. 1993, *Annu. Rev. Astron. Astrophys.*, 31, 473
 Antonucci, R. R. J. & Miller, J. S. 1985, *ApJ*, 297, 621
 Arnaud, K. A. 1996, *Astronomical Data Analysis Software and Systems V*, 101, 17
 Baloković, M., Brightman, M., Harrison, F. A., et al. 2018, *The Astrophysical Journal*, 854, 42
 Buchner, J., Brightman, M., Nandra, K., Nikutta, R., & Bauer, F. 2019, *A&A*, 629, A16
 Buchner, J., Georgakakis, A., Nandra, K., et al. 2015, *The Astrophysical Journal*, 802, 89
 Burlon, D., Ajello, M., Greiner, J., et al. 2011, *The Astrophysical Journal*, 728, 58
 Cash, W. 1979, *ApJ*, 228, 939
 Comastri, A., Setti, G., Zamorani, G., & Hasinger, G. 1995, *A&A*, 296, 1
 Evans, P. A., Beardmore, A. P., Page, K. L., et al. 2009, *Monthly Notices of the Royal Astronomical Society*, 397, 1177
 Fruscione, A., McDowell, J. C., Allen, G. E., et al. 2006, in *Society of Photo-Optical Instrumentation Engineers (SPIE) Conference Series*, Vol. 6270, Proc. SPIE, 62701V
 Furui, S., Fukazawa, Y., Odaka, H., et al. 2016, *The Astrophysical Journal*, 818, 164
 Gilli, R., Comastri, A., & Hasinger, G. 2007, *A&A*, 463, 79
 Hickox, R. C. & Alexander, D. M. 2018, *Annual Review of Astronomy and Astrophysics*, 56, 625
 Höning, S. F., Beckert, T., Ohnaka, K., & Weigelt, G. 2006, *A&A*, 452, 459
 Jansen, F., Lumb, D., Altieri, B., et al. 2001, *A&A*, 365, L1
 Kalberla, P. M. W., Burton, W. B., Hartmann, Dap, et al. 2005, *A&A*, 440, 775
 Lansbury, G. B., Alexander, D. M., Aird, J., et al. 2017, *ApJ*, 846, 20
 Liu, Y. & Li, X. 2014, *The Astrophysical Journal*, 787, 52
 Maccacaro, T., della Ceca, R., Gioia, I. M., et al. 1991, *ApJ*, 374, 117
 Madau, P., Ghisellini, G., & Fabian, A. C. 1994, *Monthly Notices of the Royal Astronomical Society*, 270, L17
 Marchesi, S., Ajello, M., Marcotulli, L., et al. 2018, *The Astrophysical Journal*, 854, 49
 Marchesi, S., Ajello, M., Zhao, X., et al. 2019, *The Astrophysical Journal*, 872, 8
 Marchesi, S., Gilli, R., Lanzuisi, G., et al. 2020, *A&A*, 642, A184

Marchesi, S., Lanzuisi, G., Civano, F., et al. 2016, *The Astrophysical Journal*, 830, 100

Markowitz, A. G., Krumpe, M., & Nikutta, R. 2014, *Monthly Notices of the Royal Astronomical Society*, 439, 1403

Mason, R. E., Levenson, N. A., Shi, Y., et al. 2009, *ApJ*, 693, L136

Matt, G. & Fabian, A. C. 1994, *Monthly Notices of the Royal Astronomical Society*, 267, 187

Mewe, R., Gronenschild, E. H. B. M., & van den Oord, G. H. J. 1985, *A&AS*, 62, 197

Nenkova, M., Ivezić, Ž., & Elitzur, M. 2002, *The Astrophysical Journal*, 570, L9

Nenkova, M., Sirocky, M. M., Ivezić, Ž., & Elitzur, M. 2008, *The Astrophysical Journal*, 685, 147

Netzer, H. 2015, *Annual Review of Astronomy and Astrophysics*, 53, 365

Noguchi, K., Terashima, Y., Ishino, Y., et al. 2010, *The Astrophysical Journal*, 711, 144

Ricci, C., Ueda, Y., Koss, M. J., et al. 2015, *The Astrophysical Journal Letters*, 815, L13

Richstone, D., Ajhar, E. A., Bender, R., et al. 1998, *Nature*, 385, A14

Risaliti, G., Elvis, M., & Nicastro, F. 2002, *The Astrophysical Journal*, 571, 234

Risaliti, G., Maiolino, R., & Salvati, M. 1999, *The Astrophysical Journal*, 522, 157

Soltan, A. 1982, *MNRAS*, 200, 115

Stalevski, M., Ricci, C., Ueda, Y., et al. 2016, *Monthly Notices of the Royal Astronomical Society*, 458, 2288

Strüder, L., Briel, U., Dennerl, K., et al. 2001, *A&A*, 365, L18

Tanimoto, A., Ueda, Y., Odaka, H., et al. 2019, *The Astrophysical Journal*, 877, 95

Turner, M. J. L., Abbey, A., Arnaud, M., et al. 2001, *A&A*, 365, L27

Ueda, Y., Akiyama, M., Hasinger, G., Miyaji, T., & Watson, M. G. 2014, *The Astrophysical Journal*, 786, 104

Verner, D., Ferland, G., Korista, K., & Yakovlev, D. 1996, *Astrophysical Journal*, 465, 487

Zappacosta, L., Comastri, A., Civano, F., et al. 2018, *The Astrophysical Journal*, 854, 33

Zhao, X., Marchesi, S., & Ajello, M. 2019a, *The Astrophysical Journal*, 871, 182

Zhao, X., Marchesi, S., Ajello, M., Baloković, M., & Fischer, T. 2020, *The Astrophysical Journal*, 894, 71

Zhao, X., Marchesi, S., Ajello, M., et al. 2019b, *The Astrophysical Journal*, 870, 60

APPENDIX

DATA REDUCTION

The *NuSTAR* data of both FPMA and FPMB are calibrated, cleaned and screened using the `nupipeline` script version 0.4.6 and calibration database (CALDB) version 20181030. The sources spectra, ancillary response files (ARF) and response matrix files (RMF) are obtained using the `nuproducts` script version 0.3.0. The sources spectra are extracted from a 75" circular region and the background spectra are extracted using a 75" circular region near the source but avoiding contamination from the source.

The XMM-*Newton* data from two MOS cameras (Turner et al. 2001) and one EPIC CCD cameras (pn; Strüder et al. 2001) on-board XMM-*Newton* are utilized in the spectral analysis. The XMM-*Newton* data are reduced using the Science Analysis System (SAS; Jansen et al. 2001) version 17.0.0 following standard procedures. The flares are removed by visually inspecting the high energy light curve (10–12 keV) when the count rates exceed 0.35 cts/s for MOS and 0.4 cts/s for pn. The source spectra are extracted from a circular region with radius of 15"; the background spectra are extracted from a circle nearby the source with the same radius as the source spectra but avoiding contamination from sources.

Chandra data, focused on the 0.3–7 keV energy band, are used in our spectral analysis when the XMM-*Newton* data are not available. We reduced the *Chandra* data using the *Chandra*'s data analysis system, CIAO software package (Fruscione et al. 2006) version 4.11 and *Chandra* CALDB version 4.8.2. The level=1 data are reprocessed using the CIAO `chandra_repro` script. The source spectrum is extracted from a circular region centered at the source with a radius of 5"; background spectrum is extracted from a circular region near the source with a radius of 10". The CIAO `specextract` tool is used to extract both source and background spectra, ARF and RMF files following standard procedures.

Given the smaller effective area in soft X-ray band (8 times smaller than XMM-*Newton* pn and 4 times smaller than *Chandra* at 3 keV), *Swift*-XRT data are used only when neither XMM-*Newton* nor *Chandra* data are available. The spectra are obtained from the online *Swift* product generator⁹ (see also Evans et al. 2009). In case of variability, we did not stack multiple observations. The *Swift*-XRT spectra are rebinned with a minimum of 5 counts per bin due to the limited number of counts, using the HEAsoft task `grppha`, while the *NuSTAR*, XMM-*Newton* and *Chandra* spectra are rebinned with a minimum of 20 counts per bin.

SPECTRAL ANALYSIS

The photoelectric cross section for absorption component in the fitting procedure is from Verner et al. (1996); the element abundance is from Anders & Grevesse (1989) and metal abundance is fixed to Solar; the Galactic absorption column density is obtained using the `nh` task (Kalberla et al. 2005) in HEAsoft for each source. The χ^2 statistic is used when XMM-*Newton* data and *Chandra* data are used, while C statistic (Cash 1979) is used when *Swift*-XRT data are applied due to the low quality of the *Swift*-XRT spectra and limited number of counts in each bin.

The reprocessed component, `borus02`, assumes a sphere with conical cutouts at both poles (Baloković et al. 2018), approximating a torus with an opening angle which can vary in the range of $\theta_{\text{Tor}} = [0-84]^\circ$, corresponding to a torus covering factor, $c_f = \cos(\theta_{\text{Tor}}) = [1-0.1]$. The inclination angle, which is the angle between the axis of the AGN and the observer line-of-sight, is also a free parameter ranging from $\theta_{\text{inc}} = [18-87]^\circ$, where $\theta_{\text{obs}} = 0^\circ$ is when the AGN is observed “face-on” and $\theta_{\text{obs}} = 90^\circ$ is observed “edge-on”. The relative iron abundance of the reprocessed component, A_{Fe} , is fixed to 1 (the solar value), except for some sources where a significant improvement has been found when A_{Fe} is free to vary. The column density of the obscuring torus in the reprocessed component is decoupled from the one of line-of-sight: the column density of the reprocessed component is an average property of the obscuring torus while the line-of-sight column density represents a quantity that is located along our line-of-sight, and could vary when observed at different epoch.

In the process of modeling the spectra, the photon indices, Γ , the cut-off energy, E_{cut} and the normalization, norm, of the intrinsic continuum, the reprocessed component and the fractional unabsorbed continuum are tied together, assuming that the three components have the same origin. The photon index in `borus02` model is in the range of [1.4–2.6], thus the photon index in the cut-off power-law is also constrained between 1.4 and 2.6. The cut-off energy is fixed at $E_{\text{cut}} = 500$ keV for all sources, except for ESO 383-18, whose cut-off energy is found to be $E_{\text{cut}} < 20$ keV. The fractional unabsorbed continuum is usually less than 5–10% of the intrinsic continuum (see, e.g., Noguchi et al. 2010; Marchesi et al. 2016). We denote this fraction as f_s , and model it with a constant (`constant2`). Finally, the spectra of some sources are found to be composed of strong non-AGN thermal emission around 1 keV, which may be caused by the star formation process and/or diffuse gas emission. We use `mekal` (Mewe et al. 1985) to model this non-AGN thermal contribution: the temperature and the relative metal abundance in `mekal` are both left free to vary.

When analyzing the spectra of 3C 445, we add a few gaussian lines to model different emission lines. For a few sources, i.e., 3C 445, 3C 452 and ESO 383-18, we let the relative iron abundance of the reprocessed component free to vary when fitting their spectra and obtain $A_{\text{Fe},3\text{C}445}$ is $0.32^{+0.05}_{-0.08}$, $A_{\text{Fe},3\text{C}452} = 0.41^{+0.05}_{-0.05}$ and $A_{\text{Fe},\text{ESO}383} = 0.19^{+0.07}_{-0.05}$, otherwise the photon indices of their intrinsic power law would be unphysical ($\Gamma > 2.5$).

⁹ http://www.swift.ac.uk/user_objects/

Table 2
Best-fit results of the sources with *NuSTAR* (3-78 keV) data & XMM-*Newton* (1-10 keV) data

Source	$\chi^2/\text{d.o.f.}$	Γ	$N_{\text{H},\text{l.o.s.}}^{\text{a}}$	$N_{\text{H},\text{tor}}^{\text{b}}$	$\cos(\theta_{\text{inc}})^{\text{c}}$	c_f^{d}	norm ^e	Flux ₂₋₁₀ ^f	$L_{\text{int},2-10}^{\text{g}}$
2MASX J06411806+3249313	382/371	$1.60^{+0.09}_{-0.08}$	$23.09^{+0.08}_{-0.10}$	$22.86^{+0.89}_{-0.34}$	0.95^{+u}_{-u}	$0.88^{+u}_{-0.76}$	$0.16^{+0.04}_{-0.03}$	$-11.27^{+0.04}_{-0.08}$	$43.70^{+0.05}_{-0.05}$
3C 105	205/232	$1.53^{+0.13}_{-0.13}$	$23.65^{+0.03}_{-0.03}$	-	-	-	$0.25^{+0.10}_{-0.07}$	$-12.03^{+0.02}_{-0.05}$	$43.97^{+0.07}_{-0.07}$
3C 445	885/913	$1.56^{+0.05}_{-0.14}$	$23.08^{+0.05}_{-0.07}$	$24.00^{+0.11}_{-0.32}$	$0.95^{+u}_{-0.08}$	$0.80^{+0.12}_{-0.20}$	$0.22^{+0.02}_{-0.04}$	$-11.27^{+0.02}_{-0.08}$	$43.76^{+0.01}_{-0.01}$
3C 452	1206/1177	$1.50^{+0.03}_{-0.02}$	$23.59^{+0.03}_{-0.01}$	$22.96^{+0.04}_{-0.08}$	$0.95^{+u}_{-0.09}$	$1.00^{+u}_{-0.12}$	$0.26^{+0.02}_{-0.01}$	$-11.51^{+0.01}_{-0.02}$	$44.36^{+0.02}_{-0.01}$
4C +29.30	168/176	$1.46^{+0.21}_{-u}$	$23.50^{+0.04}_{-0.06}$	$23.90^{+0.11}_{-0.09}$	0.55^{+u}_{-u}	$1.00^{+u}_{-0.57}$	$0.05^{+0.04}_{-0.01}$	$-12.00^{+0.01}_{-0.51}$	$43.35^{+0.13}_{-0.05}$
Cen A	5100/4781	$1.81^{+0.01}_{-0.01}$	$23.06^{+0.01}_{-0.01}$	$23.04^{+0.26}_{-0.06}$	$0.35^{+0.15}_{-0.04}$	$0.30^{+0.04}_{-0.13}$	$9.95^{+0.07}_{-0.14}$	$-9.36^{+0.01}_{-0.01}$	$42.82^{+0.01}_{-0.01}$
CGCG 427-028	463/470	$1.76^{+0.03}_{-0.09}$	$23.15^{+0.03}_{-0.04}$	$25.46^{+u}_{-1.12}$	$0.60^{+0.31}_{-0.40}$	$0.62^{+0.06}_{-0.42}$	$0.11^{+0.01}_{-0.02}$	$-11.66^{+0.02}_{-0.03}$	$42.99^{+0.03}_{-0.03}$
ESO 103-35	2006/1907	$1.70^{+0.10}_{-0.08}$	$23.25^{+0.02}_{-0.02}$	$24.36^{+0.08}_{-0.07}$	$0.51^{+0.16}_{-0.05}$	$0.65^{+0.14}_{-0.07}$	$1.73^{+0.34}_{-0.16}$	$-10.74^{+0.01}_{-0.06}$	$43.37^{+0.02}_{-0.02}$
ESO 263-13	410/444	$1.64^{+0.12}_{-0.12}$	$23.83^{+0.04}_{-0.03}$	$22.60^{+0.48}_{-0.12}$	$0.64^{+0.20}_{-u}$	$0.70^{+u}_{-0.42}$	$0.24^{+0.01}_{-0.01}$	$-11.87^{+0.01}_{-0.07}$	$43.50^{+0.04}_{-0.05}$
ESO 317-41	158/156	$1.76^{+0.31}_{-0.21}$	$23.90^{+0.07}_{-0.08}$	$24.66^{+u}_{-0.50}$	$0.45^{+0.36}_{-u}$	$0.56^{+u}_{-0.26}$	$0.12^{+0.16}_{-0.07}$	$-12.36^{+0.17}_{-u}$	$42.60^{+0.18}_{-0.29}$
ESO 383-18	1367/1343	$1.58^{+0.04}_{-0.05}$	$23.28^{+0.03}_{-0.02}$	$24.38^{+0.07}_{-0.10}$	$0.84^{+0.07}_{-0.15}$	$0.86^{+0.10}_{-0.13}$	$0.39^{+0.04}_{-0.04}$	$-11.34^{+0.02}_{-0.04}$	$42.54^{+0.03}_{-0.02}$
ESO 439-G009	173/180	$1.77^{+0.26}_{-0.19}$	$23.58^{+0.09}_{-0.09}$	$24.26^{+u}_{-0.15}$	$0.10^{+0.67}_{-u}$	$0.64^{+u}_{-0.38}$	$0.16^{+0.16}_{-0.07}$	$-11.93^{+0.17}_{-0.35}$	$42.89^{+0.14}_{-0.16}$
ESO 464-16	137/131	$1.46^{+0.30}_{-u}$	$23.79^{+0.18}_{-0.05}$	$23.96^{+0.27}_{-0.20}$	$0.74^{+0.11}_{-u}$	$0.91^{+u}_{-0.52}$	$0.04^{+0.05}_{-0.09}$	$-12.27^{+0.08}_{-u}$	$42.97^{+0.19}_{-0.10}$
Fairall 272	559/594	$1.51^{+0.11}_{-0.08}$	$23.23^{+0.05}_{-0.05}$	$24.00^{+0.33}_{-0.31}$	$0.37^{+0.21}_{-u}$	$0.40^{+0.47}_{-0.15}$	$0.18^{+0.06}_{-0.04}$	$-11.19^{+0.06}_{-0.20}$	$43.10^{+0.06}_{-0.04}$
IC 4518A	188/186	$1.72^{+0.15}_{-0.18}$	$23.11^{+0.12}_{-0.16}$	$24.28^{+0.40}_{-0.30}$	$0.75^{+0.16}_{-u}$	$0.80^{+u}_{-0.37}$	$0.20^{+0.09}_{-0.06}$	$-11.37^{+0.03}_{-0.09}$	$42.75^{+0.06}_{-0.09}$
IC 751	280/257	$2.10^{+0.11}_{-0.18}$	$23.60^{+0.03}_{-0.03}$	$24.81^{+u}_{-0.35}$	$0.75^{+0.11}_{-u}$	$0.86^{+u}_{-0.38}$	$0.28^{+0.09}_{-0.10}$	$-11.93^{+0.10}_{-0.07}$	$43.20^{+0.06}_{-0.09}$
IRAS 16288+3929	187/196	$1.72^{+0.12}_{-0.17}$	$23.88^{+0.06}_{-0.10}$	$23.42^{+0.69}_{-0.12}$	$0.26^{+0.47}_{-u}$	$0.41^{+0.44}_{-0.17}$	$0.23^{+0.11}_{-0.11}$	$-12.06^{+0.06}_{-0.07}$	$43.28^{+0.17}_{-0.19}$
LEDA 2816387	243/232	$1.33^{+0.13}_{-0.12}$	$23.76^{+0.05}_{-0.07}$	-	-	-	$0.08^{+0.04}_{-0.03}$	$-12.00^{+0.01}_{-0.09}$	$44.24^{+0.11}_{-0.10}$
LEDA 511869	157/155	$1.49^{+0.18}_{-u}$	$23.88^{+0.12}_{-0.03}$	$24.00^{+u}_{-0.70}$	$0.13^{+0.13}_{-0.06}$	$0.10^{+0.26}_{-u}$	$0.22^{+0.23}_{-0.05}$	$-11.24^{+0.03}_{-0.61}$	$43.92^{+0.07}_{-0.06}$
MCG -01-05-047	251/261	$1.89^{+0.10}_{-0.12}$	$23.33^{+0.09}_{-0.09}$	$24.46^{+u}_{-0.26}$	$0.89^{+0.05}_{-0.20}$	$0.89^{+0.07}_{-0.16}$	$0.30^{+0.08}_{-0.07}$	$-11.58^{+0.04}_{-0.06}$	$42.68^{+0.04}_{-0.04}$
MCG -02-09-040	111/92	$1.95^{+0.39}_{-0.15}$	$23.90^{+0.12}_{-0.14}$	$25.50^{+u}_{-1.14}$	$0.86^{+u}_{-0.52}$	$0.77^{+0.11}_{-0.43}$	$0.12^{+0.38}_{-0.07}$	$-12.31^{+0.01}_{-u}$	$42.26^{+0.24}_{-0.34}$
MCG -03-34-064	1920/1460	$1.92^{+0.02}_{-0.02}$	$23.77^{+0.02}_{-0.01}$	$24.53^{+0.03}_{-0.05}$	$0.85^{+0.01}_{-0.00}$	$0.86^{+0.04}_{-0.00}$	$0.48^{+0.01}_{-0.03}$	$-11.68^{+0.02}_{-0.06}$	$42.92^{+0.01}_{-0.01}$
Mrk 3	1056/1073	$1.48^{+0.11}_{-u}$	$23.94^{+0.06}_{-0.04}$	$23.30^{+0.24}_{-0.05}$	$0.47^{+0.16}_{-0.07}$	$0.50^{+0.06}_{-0.22}$	$1.42^{+0.54}_{-0.22}$	$-11.01^{+0.01}_{-0.05}$	$43.42^{+0.05}_{-0.04}$
Mrk 18	212/204	$1.70^{+0.15}_{-0.23}$	$23.13^{+0.06}_{-0.05}$	$25.10^{+u}_{-2.22}$	$0.95^{+u}_{-0.63}$	$0.25^{+0.10}_{-0.14}$	$0.07^{+0.02}_{-0.01}$	$-11.97^{+0.03}_{-0.23}$	$41.76^{+0.05}_{-0.05}$
Mrk 273	339/359	$1.76^{+0.20}_{-0.20}$	$23.52^{+0.05}_{-0.09}$	$24.11^{+0.10}_{-0.22}$	0.15^{+u}_{-u}	$1.00^{+u}_{-0.44}$	$0.06^{+0.00}_{-0.03}$	$-12.09^{+0.01}_{-0.27}$	$42.90^{+0.14}_{-0.12}$
Mrk 348	2702/2583	$1.66^{+0.03}_{-0.03}$	$22.92^{+0.03}_{-0.04}$	$24.48^{+0.48}_{-0.54}$	$0.21^{+0.02}_{-0.03}$	$0.17^{+0.08}_{-u}$	$1.33^{+0.09}_{-0.08}$	$-10.43^{+0.01}_{-0.01}$	$43.48^{+0.04}_{-0.08}$
Mrk 417	314/326	$1.57^{+0.08}_{-0.09}$	$23.53^{+0.06}_{-0.07}$	$23.15^{+1.53}_{-0.25}$	$0.15^{+0.26}_{-u}$	$0.40^{+0.21}_{-u}$	$0.23^{+0.04}_{-0.05}$	$-11.51^{+0.01}_{-0.05}$	$43.46^{+0.01}_{-0.01}$
Mrk 477	673/539	$1.58^{+0.09}_{-0.07}$	$23.30^{+0.06}_{-0.07}$	$22.90^{+0.14}_{-0.20}$	0.95^{+u}_{-u}	$1.00^{+u}_{-0.22}$	$0.16^{+0.06}_{-0.03}$	$-11.47^{+0.01}_{-0.01}$	$43.36^{+0.05}_{-0.05}$
Mrk 1210	679/669	$1.77^{+0.06}_{-0.03}$	$23.30^{+0.04}_{-0.02}$	$24.11^{+0.11}_{-0.08}$	0.95^{+u}_{-u}	$1.00^{+u}_{-0.07}$	$0.74^{+0.15}_{-0.11}$	$-11.12^{+0.01}_{-0.02}$	$42.92^{+0.03}_{-0.03}$
Mrk 1498	811/815	$1.67^{+0.04}_{-0.04}$	$23.26^{+0.02}_{-0.03}$	$23.00^{+0.63}_{-0.70}$	$0.95^{+u}_{-0.62}$	$0.32^{+0.62}_{-u}$	$0.42^{+0.05}_{-0.05}$	$-11.10^{+0.01}_{-0.02}$	$44.12^{+0.02}_{-0.02}$
NGC 454E	344/310	$1.81^{+0.11}_{-0.11}$	$23.86^{+0.04}_{-0.04}$	$24.75^{+0.68}_{-0.40}$	$0.43^{+0.16}_{-0.11}$	$0.40^{+0.26}_{-0.24}$	$0.16^{+0.06}_{-0.03}$	$-12.18^{+0.02}_{-0.15}$	$42.26^{+0.04}_{-0.04}$
NGC 612	176/195	$1.54^{+0.12}_{-0.08}$	$23.95^{+0.05}_{-0.04}$	$23.78^{+0.18}_{-0.29}$	$0.05^{+0.01}_{-u}$	$0.10^{+0.20}_{-u}$	$0.53^{+0.30}_{-0.02}$	$-11.96^{+0.02}_{-0.21}$	$43.56^{+0.14}_{-0.02}$
NGC 788	303/290	$1.56^{+0.14}_{-0.16}$	$23.79^{+0.04}_{-0.05}$	$24.50^{+u}_{-1.11}$	$0.26^{+0.08}_{-0.03}$	$0.20^{+0.25}_{-u}$	$0.45^{+0.18}_{-0.15}$	$-11.71^{+0.01}_{-0.25}$	$42.97^{+0.07}_{-0.10}$
NGC 835	104/124	$1.40^{+0.25}_{-u}$	$23.46^{+0.09}_{-0.06}$	$23.22^{+0.16}_{-0.31}$	$0.05^{+0.34}_{-u}$	$0.40^{+0.20}_{-0.10}$	$0.04^{+0.01}_{-0.01}$	$-12.09^{+0.12}_{-0.58}$	$41.81^{+0.02}_{-0.08}$
NGC 1142	225/255	$1.48^{+0.16}_{-u}$	$24.20^{+0.08}_{-0.07}$	$23.49^{+0.15}_{-0.13}$	$0.05^{+0.28}_{-u}$	$0.45^{+0.14}_{-0.05}$	$0.36^{+0.17}_{-0.08}$	$-12.10^{+0.04}_{-0.16}$	$43.44^{+0.13}_{-0.11}$
NGC 2655	123/120	$2.12^{+0.23}_{-0.17}$	$23.51^{+0.08}_{-0.08}$	23.65^{+u}_{-u}	$0.15^{+0.64}_{-u}$	0.39^{+u}_{-u}	$0.22^{+0.02}_{-0.10}$	$-11.96^{+0.07}_{-2.54}$	$41.37^{+0.18}_{-0.16}$
NGC 3281	506/495	$1.77^{+0.12}_{-0.09}$	$24.30^{+0.06}_{-0.06}$	$25.50^{+u}_{-0.08}$	$0.55^{+0.13}_{-0.09}$	$0.52^{+0.12}_{-0.13}$	$0.68^{+0.31}_{-0.19}$	$-11.72^{+0.12}_{-0.23}$	$42.98^{+0.11}_{-0.10}$
NGC 4258	1577/1582	$1.92^{+0.08}_{-0.05}$	$22.94^{+0.02}_{-0.02}$	$23.49^{+0.26}_{-0.15}$	$0.95^{+u}_{-0.05}$	$0.90^{+0.05}_{-0.05}$	$0.21^{+0.03}_{-0.02}$	$-11.66^{+0.01}_{-0.03}$	$40.23^{+0.02}_{-0.01}$
NGC 4507	1383/1355	$1.63^{+0.05}_{-0.04}$	$23.87^{+0.02}_{-0.02}$	$22.90^{+0.16}_{-0.09}$	$0.51^{+0.11}_{-u}$	$0.66^{+0.12}_{-0.18}$	$1.49^{+0.32}_{-0.20}$	$-10.97^{+0.01}_{-0.01}$	$43.33^{+0.03}_{-0.04}$
NGC 4785	402/364	$1.96^{+0.15}_{-0.15}$	$23.70^{+0.04}_{-0.04}$	$24.43^{+0.37}_{-0.37}$	$0.63^{+0.22}_{-0.05}$	$0.70^{+u}_{-0.11}$	$0.21^{+0.12}_{-0.08}$	$-12.04^{+0.12}_{-0.07}$	$42.32^{+0.07}_{-0.12}$
NGC 4992	480/449	$1.50^{+0.06}_{-0.05}$	$23.46^{+0.03}_{-0.03}$	$24.00^{+0.04}_{-0.07}$	0.25^{+u}_{-u}	$1.00^{+u}_{-0.22}$	$0.18^{+0.05}_{-0.03}$	$-11.54^{+0.01}_{-0.14}$	$43.10^{+0.04}_{-0.06}$
NGC 5899	820/866	$1.99^{+0.03}_{-0.02}$	$23.08^{+0.01}_{-0.01}$	$24.79^{+0.13}_{-0.15}$	$0.95^{+u}_{-0.02}$	$0.95^{+0.01}_{-0.01}$	$0.43^{+0.01}_{-0.01}$	$-11.27^{+0.01}_{-0.02}$	$42.26^{+0.01}_{-0.01}$
NGC 6300	863/952	$1.90^{+0.05}_{-0.08}$	$23.21^{+0.03}_{-0.05}$	$24.40^{+0.16}_{-0.10}$	$0.73^{+0.13}_{-0.14}$	$0.81^{+0.13}_{-0.14}$	$0.11^{+0.02}_{-0.02}$	$-10.81^{+0.03}_{-0.01}$	$42.08^{+0.02}_{-0.03}$
NGC 7319	387/346	$1.71^{+0.09}_{-0.21}$	$23.81^{+0.04}_{-0.05}$	$25.50^{+u}_{-0.38}$	$0.69^{+0.20}_{-0.08}$	$0.70^{+0.05}_{-0.26}$	$0.27^{+0.10}_{-0.12}$	$-12.39^{+0.08}_{-0.15}$	$42.56^{+0.08}_{-0.10}$
PKS 2356-61	296/294	$1.90^{+0.04}_{-0.09}$	$23.23^{+0.03}_{-0.03}$	$25.50^{+u}_{-1.26}$	$0.76^{+0.17}_{-0.08}$	$0.76^{+0.07}_{-0.41}$	$0.21^{+0.02}_{-0.05}$	$-11.57^{+0.01}_{-0.06}$	$44.26^{+0.03}_{-0.03}$
SDSS J165315+234942	307/350	$1.50^{+0.09}_{-0.06}$	$23.20^{+0.06}_{-0.05}$	$22.95^{+1.33}_{-0.65}$	$0.95^{+u}_{-0.80}$	0.70^{+u}_{-u}	$0.08^{+0.02}_{-0.01}$	$-11.70^{+0.03}_{-0.07}$	$44.01^{+0.04}_{-0.05}$
VII Zw73	93/96	$1.78^{+0.27}_{-0.26}$	$23.81^{+0.08}_{-0.09}$	-	-	-	$0.21^{+0.28}_{-0.12}$	$-12.17^{+0.05}_{-0.31}$	$43.49^{+0.20}_{-0.19}$
WISE J144850.99-400845.6	1247/1099	$1.60^{+0.03}_{-0.04}$	$22.45^{+0.03}_{-0.03}$	-	-	-	$0.12^{+0.01}_{-0.01}$	-11.2	

Table 3
Best-fit results of the sources with *NuSTAR* (3-78 keV) data & *Chandra* (1-7 keV) data

Source	$\chi^2/\text{d.o.f.}$	Γ	$N_{\text{H, l.o.s.}}^{\text{a}}$	$N_{\text{H, tor}}^{\text{b}}$	$\cos(\theta_{\text{inc}})^{\text{c}}$	c_{f}^{d}	norm ^e	Flux ₂₋₁₀ ^f	L _{int, 2-10} ^g
2MASX J01073963-1139117	10/18	$1.82_{-0.20}^{+0.50}$	$24.48_{-0.05}^{+u}$	$23.47_{-0.38}^{+0.29}$	0.05_{-u}^{+u}	0.10_{-u}^{+u}	$1.13_{-0.12}^{+4.69}$	$-12.33_{-u}^{+0.15}$	$44.30_{-0.93}^{+1.44}$
3C 403	358/305	$2.11_{-0.11}^{+0.09}$	$23.65_{-0.03}^{+0.03}$	$24.76_{-0.38}^{+u}$	$0.56_{-0.15}^{+0.25}$	$0.60_{-0.14}^{+0.28}$	$0.67_{-0.18}^{+0.19}$	$-11.64_{-0.03}^{+0.05}$	$44.09_{-0.05}^{+0.05}$
4C +73.08	139/135	$1.40_{-u}^{+0.12}$	$23.53_{-0.12}^{+0.04}$	$22.93_{-0.47}^{+0.21}$	0.05_{-u}^{+u}	$0.70_{-0.31}^{+u}$	$0.08_{-0.01}^{+0.00}$	$-11.81_{-0.31}^{+0.10}$	$43.60_{-0.05}^{+0.02}$
CASG 218	201/209	$1.60_{-0.14}^{+0.19}$	$23.41_{-0.08}^{+0.04}$	$24.13_{-1.48}^{+u}$	0.35_{-u}^{+u}	$0.20_{-u}^{+0.71}$	$0.11_{-0.04}^{+0.06}$	$-11.73_{-0.15}^{+0.04}$	$43.55_{-0.10}^{+0.08}$
ESO 119-8	91/106	$1.66_{-0.17}^{+0.18}$	$23.17_{-0.09}^{+0.09}$	-	-	-	$0.03_{-0.01}^{+0.02}$	$-12.19_{-0.07}^{+0.03}$	$42.25_{-0.07}^{+0.08}$
ESO 500-34	115/120	$2.34_{-0.43}^{+0.25}$	$23.67_{-0.05}^{+0.09}$	$24.17_{-0.45}^{+u}$	$0.15_{-u}^{+0.71}$	$0.88_{-0.68}^{+u}$	$0.62_{-0.42}^{+0.72}$	$-11.92_{-0.56}^{+0.15}$	$42.52_{-0.27}^{+0.17}$
IC 5063	732/742	$1.77_{-0.07}^{+0.08}$	$23.36_{-0.02}^{+0.02}$	$24.31_{-0.21}^{+0.24}$	$0.48_{-0.11}^{+0.16}$	$0.53_{-0.15}^{+0.22}$	$0.71_{-0.12}^{+0.14}$	$-11.06_{-0.02}^{+0.02}$	$42.87_{-0.03}^{+0.03}$
LEDA 15023	78/77	$1.91_{-0.25}^{+0.25}$	$23.97_{-0.18}^{+0.08}$	$23.18_{-0.28}^{+0.18}$	$0.05_{-u}^{+0.12}$	$0.18_{-u}^{+0.12}$	$0.88_{-0.51}^{+1.23}$	$-11.86_{-0.52}^{+0.03}$	$44.09_{-0.11}^{+0.10}$
NGC 4102	297/300	$1.74_{-0.08}^{+0.12}$	$23.87_{-0.03}^{+0.04}$	$25.15_{-0.68}^{+u}$	$0.53_{-0.24}^{+0.16}$	$0.61_{-0.22}^{+0.31}$	$0.46_{-0.12}^{+0.22}$	$-11.84_{-0.04}^{+0.31}$	$41.49_{-0.06}^{+0.09}$
NGC 4388	953/871	$1.64_{-0.08}^{+0.05}$	$23.43_{-0.02}^{+0.02}$	$24.00_{-0.20}^{+0.07}$	$0.60_{-0.04}^{+0.15}$	$0.60_{-0.05}^{+0.16}$	$0.49_{-0.09}^{+0.06}$	$-11.14_{-0.02}^{+0.01}$	$42.52_{-0.03}^{+0.03}$
NGC 4939	228/234	$1.69_{-0.15}^{+0.19}$	$23.82_{-0.08}^{+0.09}$	$23.02_{-0.14}^{+0.13}$	$0.05_{-u}^{+0.45}$	$0.57_{-0.14}^{+0.13}$	$0.31_{-0.13}^{+0.30}$	$-11.80_{-0.15}^{+0.01}$	$42.49_{-0.13}^{+0.16}$
NGC 4941	106/111	$1.40_{-u}^{+0.31}$	$23.98_{-0.20}^{+0.30}$	$24.50_{-0.68}^{+0.44}$	$0.65_{-0.20}^{+u}$	$0.40_{-0.23}^{+0.43}$	$0.06_{-0.03}^{+0.01}$	$-12.28_{-u}^{+0.06}$	$41.04_{-0.46}^{+0.43}$
NGC 5283	343/302	$1.81_{-0.17}^{+0.16}$	$23.04_{-0.09}^{+0.11}$	$24.39_{-0.80}^{+u}$	$0.60_{-0.19}^{+u}$	$0.50_{-0.32}^{+u}$	$0.13_{-0.04}^{+0.05}$	$-11.62_{-0.11}^{+0.01}$	$42.02_{-0.06}^{+0.06}$
NGC 5972	177/188	$1.75_{-0.21}^{+0.36}$	$23.79_{-0.07}^{+0.13}$	$24.34_{-0.18}^{+u}$	$0.85_{-0.33}^{+0.03}$	$0.90_{-0.32}^{+u}$	$0.08_{-0.03}^{+0.22}$	$-12.35_{-u}^{+0.10}$	$42.79_{-0.09}^{+0.07}$
SDSS J135429.05+132757.2	113/149	$1.61_{-0.15}^{+0.16}$	$23.45_{-0.11}^{+0.09}$	-	-	-	$0.11_{-0.04}^{+0.07}$	$-11.83_{-0.07}^{+0.01}$	$43.67_{-0.10}^{+0.11}$
UGC 3995B	234/258	$1.61_{-0.09}^{+0.05}$	$23.48_{-0.02}^{+0.04}$	$24.25_{-0.16}^{+0.08}$	$0.87_{-u}^{+0.05}$	$0.94_{-0.18}^{+u}$	$0.15_{-0.03}^{+0.07}$	$-11.68_{-0.19}^{+0.02}$	$42.58_{-0.15}^{+0.03}$
UGC 4211	295/304	$1.77_{-0.09}^{+0.11}$	$22.95_{-0.05}^{+0.05}$	$23.43_{-0.58}^{+0.41}$	0.05_{-u}^{+u}	$0.70_{-0.60}^{+u}$	$0.15_{-0.03}^{+0.07}$	$-11.38_{-0.13}^{+0.01}$	$43.28_{-0.05}^{+0.04}$

^aLogarithm of line-of-sight column density in cm^{-2} . If line-of-sight variability is found, the line-of-sight column density measured using *NuSTAR* data are reported

^bLogarithm of average column density of the torus in cm^{-2}

^cInclination angle, i.e., the angle between the axis of the torus and the edge of the torus

^dCovering factor of the torus

^enormalization of the main cut-off power-law component at 1 keV in 10^{-2} photons $\text{keV}^{-1} \text{cm}^{-2} \text{s}^{-1}$

^fLogarithm of flux of *NuSTAR* observation between 2-10 keV in $10^{-12} \text{erg cm}^{-2} \text{s}^{-1}$

^gLogarithm of intrinsic luminosity of *NuSTAR* observation between 2-10 keV in erg s^{-1} at 1σ confidence level

Table 4
Best-fit results of the sources with *NuSTAR* (3-78 keV) data & *Swift*-XRT (1-10 keV) data

Source	C/d.o.f.	Γ	$N_{\text{H},\text{l.o.s}}^{\text{a}}$	$N_{\text{H},\text{tor}}^{\text{b}}$	$\cos(\theta_{\text{inc}})^{\text{c}}$	c_{f}^{d}	norm ^e	Flux ₂₋₁₀ ^f	L _{int,2-10} ^g
2MASX J00502684+8229000	128/160	$2.02^{+0.21}_{-0.22}$	$23.21^{+0.19}_{-0.17}$	$24.15^{+0.17}_{-0.37}$	0.95^{+u}_{-u}	$0.98^{+u}_{-0.17}$	$0.17^{+0.15}_{-0.07}$	$-11.72^{+0.05}_{-0.07}$	$43.13^{+0.48}_{-0.27}$
2MASX J09235371-3141305	183/148	$1.36^{+0.14}_{-0.12}$	$23.66^{+0.08}_{-0.07}$	-	-	-	$0.13^{+0.08}_{-0.05}$	$-11.81^{+0.02}_{-0.06}$	$43.56^{+0.11}_{-0.11}$
2MASX J11140245+2023140	106/109	$1.53^{+0.27}_{-0.25}$	$23.70^{+0.11}_{-0.13}$	-	-	-	$0.08^{+0.12}_{-0.05}$	$-12.18^{+0.01}_{-0.68}$	$42.83^{+0.21}_{-0.19}$
ESO 21-4	215/180	$1.57^{+0.15}_{-0.14}$	$23.43^{+0.10}_{-0.10}$	-	-	-	$0.12^{+0.08}_{-0.04}$	$-11.75^{+0.02}_{-0.05}$	$42.11^{+0.11}_{-0.10}$
ESO 121-28	289/303	$2.07^{+0.08}_{-0.08}$	$23.40^{+0.05}_{-0.08}$	$24.25^{+0.04}_{-0.19}$	0.35^{+u}_{-u}	$1.00^{+u}_{-0.29}$	$0.53^{+0.15}_{-0.20}$	$-11.47^{+0.02}_{-0.08}$	$43.67^{+0.05}_{-0.10}$
ESO 231-26	296/309	$1.75^{+0.18}_{-0.14}$	$23.38^{+0.07}_{-0.08}$	$24.50^{+u}_{-0.48}$	$0.25^{+0.34}_{-u}$	$0.40^{+0.37}_{-u}$	$0.27^{+0.15}_{-0.12}$	$-11.50^{+0.04}_{-0.06}$	$43.96^{+0.09}_{-0.10}$
ESO 505-30	292/299	$1.83^{+0.18}_{-0.13}$	$23.08^{+0.10}_{-0.08}$	$24.19^{+0.20}_{-0.33}$	$0.05^{+0.53}_{-u}$	$0.50^{+0.43}_{-0.19}$	$0.19^{+0.04}_{-0.04}$	$-11.41^{+0.05}_{-0.05}$	$43.48^{+0.06}_{-0.06}$
ESO 553-43	488/493	$1.63^{+0.05}_{-0.05}$	$23.18^{+0.06}_{-0.04}$	-	-	-	$0.34^{+0.05}_{-0.05}$	$-11.19^{+0.01}_{-0.01}$	$43.42^{+0.03}_{-0.03}$
IC 1657	161/143	$1.58^{+0.36}_{-u}$	$23.53^{+0.21}_{-0.21}$	$24.11^{+u}_{-1.09}$	$0.67^{+0.24}_{-0.36}$	$0.70^{+u}_{-0.58}$	$0.07^{+0.06}_{-0.03}$	$-11.94^{+0.04}_{-u}$	$42.00^{+0.28}_{-0.19}$
IC 4709	353/326	$1.81^{+0.16}_{-0.15}$	$23.38^{+0.02}_{-0.12}$	$24.16^{+0.08}_{-0.22}$	0.95^{+u}_{-u}	$0.98^{+u}_{-0.06}$	$0.32^{+0.21}_{-0.11}$	$-11.42^{+0.04}_{-0.09}$	$42.77^{+0.07}_{-0.05}$
IRAS 05581+0006	201/199	$1.47^{+0.22}_{-u}$	$23.32^{+0.11}_{-0.12}$	$24.00^{+u}_{-0.32}$	$0.35^{+0.44}_{-u}$	0.50^{+u}_{-u}	$0.08^{+0.05}_{-0.02}$	$-11.72^{+0.04}_{-0.51}$	$44.15^{+0.12}_{-0.08}$
IRAS 20247-7542	446/401	$1.62^{+0.07}_{-0.11}$	$23.02^{+0.07}_{-0.08}$	$24.03^{+0.17}_{-0.16}$	$0.90^{+u}_{-0.41}$	$0.35^{+0.54}_{-u}$	$0.11^{+0.02}_{-0.02}$	$-11.49^{+0.05}_{-0.04}$	$44.23^{+0.04}_{-0.05}$
LEDA 2265450	222/224	$1.66^{+0.11}_{-0.11}$	$23.46^{+0.06}_{-0.06}$	-	-	-	$0.22^{+0.09}_{-0.06}$	$-11.62^{+0.01}_{-0.03}$	$43.18^{+0.03}_{-0.02}$
LEDA 46599	299/263	$1.88^{+0.21}_{-0.26}$	$23.40^{+0.08}_{-0.12}$	$24.82^{+u}_{-2.12}$	$0.91^{+u}_{-0.38}$	$0.43^{+0.32}_{-u}$	$0.26^{+0.10}_{-0.07}$	$-11.54^{+0.01}_{-0.11}$	$43.35^{+0.11}_{-0.11}$
LEDA 259433	190/196	$1.80^{+0.18}_{-0.01}$	$23.07^{+0.15}_{-0.21}$	$24.10^{+0.25}_{-0.30}$	0.05^{+u}_{-u}	$1.00^{+u}_{-0.17}$	$0.12^{+0.08}_{-0.05}$	$-11.65^{+0.01}_{-0.17}$	$43.93^{+0.09}_{-0.08}$
LEDA 549777	196/187	$1.58^{+0.10}_{-0.10}$	$23.11^{+0.07}_{-0.11}$	-	-	-	$0.07^{+0.03}_{-0.01}$	$-11.75^{+0.01}_{-0.03}$	$43.39^{+0.06}_{-0.05}$
MCG+11-11-32	117/133	$1.88^{+0.09}_{-0.10}$	$23.11^{+0.09}_{-0.07}$	$24.34^{+0.25}_{-0.19}$	0.65^{+u}_{-u}	$1.00^{+u}_{-0.32}$	$0.50^{+0.16}_{-0.12}$	$-11.16^{+0.03}_{-0.08}$	$43.67^{+0.04}_{-0.07}$
MCG-02-15-004	127/120	$2.14^{+0.42}_{-0.07}$	$23.74^{+0.05}_{-0.11}$	$24.25^{+0.17}_{-0.22}$	0.87^{+u}_{-u}	$0.98^{+u}_{-0.50}$	$0.46^{+0.08}_{-0.02}$	$-11.77^{+0.09}_{-u}$	$43.30^{+0.15}_{-0.09}$
NGC 1229	115/135	$1.45^{+0.34}_{-u}$	$23.32^{+0.14}_{-0.09}$	$24.31^{+u}_{-0.28}$	$0.86^{+u}_{-0.37}$	$0.80^{+u}_{-0.53}$	$0.03^{+0.08}_{-0.00}$	$-12.11^{+0.03}_{-u}$	$42.77^{+0.20}_{-0.09}$
NGC 4500	40/30	$1.54^{+0.58}_{-u}$	$23.36^{+0.21}_{-0.46}$	$23.52^{+0.78}_{-u}$	0.95^{+u}_{-u}	0.71^{+u}_{-u}	$0.01^{+0.02}_{-0.01}$	$-12.41^{+0.03}_{-u}$	$41.24^{+0.58}_{-0.18}$
NGC 6232	14/14	$1.40^{+0.59}_{-u}$	$23.72^{+0.51}_{-0.08}$	$24.75^{+u}_{-0.81}$	0.55^{+u}_{-u}	$0.90^{+u}_{-0.74}$	$0.01^{+0.00}_{-0.01}$	$-12.68^{+0.69}_{-u}$	$41.56^{+0.09}_{-0.60}$
UGC 3157	121/134	$2.21^{+0.34}_{-0.26}$	$23.85^{+0.07}_{-0.04}$	$24.84^{+0.10}_{-0.29}$	$0.91^{+u}_{-0.06}$	$1.00^{+u}_{-0.32}$	$0.82^{+1.44}_{-0.03}$	$-11.93^{+0.07}_{-u}$	$42.91^{+0.16}_{-0.02}$
UGC 3752	149/129	$2.03^{+0.01}_{-0.02}$	$24.00^{+0.01}_{-0.03}$	$24.58^{+0.09}_{-0.10}$	$0.90^{+0.02}_{-0.01}$	$0.91^{+0.08}_{-0.38}$	$0.43^{+0.02}_{-0.02}$	$-12.22^{+0.05}_{-u}$	$42.77^{+0.01}_{-0.02}$
Was49b	215/171	$1.49^{+0.13}_{-0.12}$	$23.30^{+0.11}_{-0.10}$	-	-	-	$0.08^{+0.04}_{-0.02}$	$-11.69^{+0.07}_{-0.06}$	$43.65^{+0.10}_{-0.09}$
Z319-7	133/113	$1.39^{+0.17}_{-0.15}$	$23.18^{+0.14}_{-0.23}$	-	-	-	$0.05^{+0.03}_{-0.02}$	$-11.82^{+0.03}_{-0.09}$	$43.14^{+0.11}_{-0.09}$
Z333-49	213/192	$1.67^{+0.13}_{-0.12}$	$23.20^{+0.10}_{-0.09}$	-	-	-	$0.10^{+0.04}_{-0.03}$	$-11.77^{+0.02}_{-0.03}$	$43.02^{+0.07}_{-0.07}$
Z367-9	196/203	$1.66^{+0.13}_{-0.16}$	$23.11^{+0.12}_{-0.21}$	$23.75^{+0.13}_{-0.24}$	0.05^{+u}_{-u}	0.59^{+u}_{-u}	$0.04^{+0.02}_{-0.01}$	$-11.89^{+0.01}_{-0.14}$	$42.41^{+0.05}_{-0.08}$

^aLogarithm of line-of-sight column density in cm⁻². If line-of-sight variability is found, the line-of-sight column density measured using *NuSTAR* data are reported

^bLogarithm of average column density of the torus in cm⁻²

^cInclination angle, i.e., the angle between the axis of the torus and the edge of the torus

^dCovering factor of the torus

^enormalization of the main cut-off power-law component at 1 keV in 10⁻² photons keV⁻¹ cm⁻² s⁻¹

^fLogarithm of flux of *NuSTAR* observation between 2-10 keV in 10⁻¹² erg cm⁻² s⁻¹

^gLogarithm of intrinsic luminosity of *NuSTAR* observation between 2-10 keV in erg s⁻¹ at 1 σ confidence level

Table 5
Reanalysis best-fit results of the CT-AGN in Marchesi et al. (2019)

Source	Statistics ^a	Γ	$N_{\text{H, l.o.s}}^{\text{b}}$	$N_{\text{H, tor}}^{\text{c}}$	$\cos(\theta_{\text{inc}})^{\text{d}}$	c_{f}^{e}	norm ^f	Flux ₂₋₁₀ ^g	$L_{\text{int, 2-10}}^{\text{h}}$
CGCG 164-19	38/37	$1.67^{+0.34}_{-u}$	$23.77^{+0.18}_{-0.16}$	$24.56^{+u}_{-0.38}$	0.89^{+u}_{-u}	$0.90^{+u}_{-0.73}$	$0.05^{+0.10}_{-0.05}$	$-12.36^{+0.33}_{-u}$	$42.61^{+0.17}_{-0.34}$
ESO 005-G004	59/47	$1.90^{+u}_{-0.40}$	$24.67^{+0.37}_{-0.37}$	$24.15^{+0.28}_{-0.29}$	$0.78^{+0.15}_{-0.45}$	$0.79^{+0.14}_{-0.47}$	$0.32^{+2.78}_{-0.32}$	$-12.27^{+0.06}_{-u}$	$41.92^{+0.49}_{-0.23}$
ESO 201-004	99/92	$1.97^{+0.28}_{-0.35}$	$24.34^{+0.09}_{-0.14}$	$23.28^{+0.08}_{-0.12}$	$0.05^{+0.18}_{-u}$	$0.20^{+0.26}_{-u}$	$0.99^{+1.23}_{-0.63}$	$-12.38^{+0.03}_{-u}$	$43.90^{+0.45}_{-0.32}$
MCG +08-03-018	125/131	$1.98^{+0.09}_{-0.12}$	$23.97^{+0.09}_{-0.09}$	$23.00^{+0.13}_{-0.23}$	0.55^{+u}_{-u}	$1.00^{+u}_{-0.64}$	$0.49^{+0.22}_{-0.30}$	$-11.89^{+0.07}_{-0.13}$	$43.08^{+0.10}_{-0.29}$
NGC 424	422/335	$2.12^{+0.04}_{-0.04}$	$24.51^{+0.02}_{-0.02}$	$23.81^{+0.05}_{-0.07}$	$0.06^{+0.01}_{-u}$	$0.10^{+0.01}_{-u}$	$5.27^{+1.59}_{-2.76}$	$-12.00^{+0.12}_{-0.64}$	$43.54^{+0.06}_{-0.06}$
NGC 1194	275/267	$1.91^{+0.11}_{-0.18}$	$23.99^{+0.05}_{-0.07}$	$24.75^{+u}_{-0.37}$	$0.86^{+0.07}_{-0.16}$	$0.85^{+0.06}_{-0.20}$	$0.39^{+0.16}_{-0.20}$	$-11.97^{+0.04}_{-u}$	$42.71^{+0.07}_{-0.09}$
NGC 3079	111/111	$2.04^{+0.20}_{-0.22}$	$24.75^{+u}_{-0.37}$	$23.81^{+0.05}_{-0.07}$	$0.15^{+0.18}_{-0.10}$	$0.23^{+0.20}_{-0.04}$	$4.07^{+8.00}_{-4.07}$	$-12.28^{+0.44}_{-u}$	$42.71^{+0.45}_{-1.10}$
NGC 3393	120/110	$1.60^{+0.20}_{-0.17}$	$24.27^{+0.24}_{-0.13}$	$24.21^{+0.05}_{-0.16}$	$0.05^{+0.64}_{-u}$	$0.55^{+0.37}_{-0.42}$	$0.43^{+0.40}_{-0.20}$	$-12.43^{+0.18}_{-2.51}$	$42.85^{+0.80}_{-0.67}$
NGC 4945	1144/1167	$1.92^{+0.02}_{-0.02}$	$24.55^{+0.01}_{-0.01}$	$24.65^{+0.04}_{-0.03}$	$0.05^{+0.01}_{-u}$	$0.12^{+0.01}_{-0.01}$	$76.86^{+0.76}_{-0.76}$	$-11.54^{+0.10}_{-0.15}$	$43.24^{+0.01}_{-0.01}$
NGC 5100	178/171	$1.69^{+0.04}_{-0.13}$	$23.29^{+0.02}_{-0.09}$	$25.50^{+u}_{-0.23}$	$0.95^{+u}_{-0.52}$	$0.25^{+0.05}_{-0.13}$	$0.17^{+0.06}_{-0.01}$	$-11.53^{+0.23}_{-0.09}$	$43.21^{+0.06}_{-0.04}$
NGC 5643	191/173	$1.63^{+0.16}_{-0.14}$	>24.24	$24.07^{+0.06}_{-0.20}$	$0.95^{+u}_{-0.59}$	$0.80^{+0.11}_{-0.24}$	$0.12^{+0.03}_{-0.02}$	$-12.13^{+0.11}_{-2.04}$	$41.35^{+0.06}_{-0.02}$
NGC 5728	417/446	$1.80^{+0.02}_{-0.10}$	$24.09^{+0.03}_{-0.01}$	$25.21^{+u}_{-0.61}$	$0.52^{+0.21}_{-0.01}$	$0.59^{+0.00}_{-0.11}$	$1.80^{+0.92}_{-0.03}$	$-11.78^{+0.52}_{-0.15}$	$43.08^{+0.09}_{-0.04}$
NGC 6240	494/476	$1.69^{+0.08}_{-0.05}$	$24.08^{+0.05}_{-0.05}$	$24.16^{+0.20}_{-0.04}$	$0.25^{+0.21}_{-u}$	$0.50^{+0.21}_{-0.21}$	$0.73^{+0.26}_{-0.15}$	$-11.64^{+0.23}_{-0.14}$	$43.67^{+0.15}_{-0.12}$
NGC 7130	81/81	$1.71^{+0.43}_{-u}$	>24.16	$24.61^{+u}_{-0.32}$	$0.28^{+0.62}_{-0.17}$	$0.37^{+0.61}_{-0.23}$	$0.37^{+1.63}_{-0.33}$	$-12.67^{+0.06}_{-1.31}$	$42.93^{+0.66}_{-u}$
NGC 7212	110/106	$2.22^{+0.04}_{-0.29}$	$24.28^{+0.12}_{-0.11}$	$23.86^{+0.99}_{-0.19}$	$0.15^{+0.02}_{-0.06}$	$0.10^{+0.33}_{-u}$	$2.36^{+3.83}_{-0.61}$	$-12.25^{+0.01}_{-1.97}$	$43.78^{+0.12}_{-0.24}$
NGC 7479	195/165	$2.29^{+0.26}_{-0.25}$	$24.76^{+0.08}_{-0.07}$	$25.08^{+u}_{-0.16}$	$0.15^{+0.01}_{-0.01}$	$0.29^{+0.01}_{-0.01}$	$46.80^{+49.59}_{-24.72}$	$-12.62^{+0.19}_{-2.37}$	$44.18^{+0.17}_{-0.22}$
NGC 7582	1708/1544	$1.64^{+0.02}_{-0.03}$	$24.23^{+0.02}_{-0.04}$	$23.29^{+0.02}_{-0.06}$	$0.25^{+0.07}_{-0.06}$	$0.90^{+u}_{-0.11}$	$0.76^{+0.01}_{-0.07}$	$-11.30^{+0.06}_{-0.06}$	$42.57^{+0.01}_{-0.01}$

^a $\chi^2/\text{d.o.f.}$ for spectra with XMM-Newton data and cstat/d.o.f. for spectra with *Swift*-XRT data.

^bLogarithm of line-of-sight column density in cm^{-2} . If line-of-sight variability is found, the line-of-sight column density measured using *NuSTAR* data are reported

^cLogarithm of average column density of the torus in cm^{-2}

^dInclination angle, i.e., the angle between the axis of the torus and the edge of the torus

^eCovering factor of the torus

^fnormalization of the main cut-off power-law component at 1 keV in 10^{-2} photons $\text{keV}^{-1} \text{cm}^{-2} \text{s}^{-1}$

^gLogarithm of flux of *NuSTAR* observation between 2–10 keV in $10^{-12} \text{erg cm}^{-2} \text{s}^{-1}$

^hLogarithm of intrinsic luminosity of *NuSTAR* observation between 2–10 keV in erg s^{-1} at 1σ confidence level